Direct numerical simulation of particle sedimentation in a Bingham fluid

A. R. Koblitz,[1,*] S. Lovett,[2] and N. Nikiforakis[3]
[1]*Department of Physics, Cavendish Laboratory, J J Thomson Avenue, Cambridge CB3 0HE, United Kingdom*
[2]*Schlumberger Cambridge Research Limited, High Cross, Madingley Road, Cambridge CB3 0EL, United Kingdom*
[3]*Department of Physics, Cavendish Laboratory, J J Thomson Avenue, Cambridge CB3 0HE, United Kingdom*

(Received 14 June 2018; published 24 September 2018)

The settling efficiency, and stability with respect to settling, of a dilute suspension of infinite circular cylinders in a quiescent viscoplastic fluid is examined by means of direct numerical simulations with varying solid volume fraction, ϕ, and yield number, Y. For Y sufficiently large we find higher settling efficiency for increasing ϕ, similar to what is found in shear-thinning fluids and opposite to what is found in Newtonian fluids. The critical yield number at which the suspension is held stationary in the carrier fluid is found to increase monotonically with ϕ, while the transition to settling is found to be diffuse: in the same suspension, particle clusters may settle while more isolated particles remain arrested. In this regime, complex flow features are observed in the sedimenting suspension, including the mobilization of lone particles by nearby sedimentation clusters. Understanding this regime, and the transition to a fully arrested state, is relevant to many industrial and natural problems involving the sedimentation of viscoplastic suspensions under quiescent flow conditions.

DOI: 10.1103/PhysRevFluids.3.093302

I. INTRODUCTION

The dispersion of coarse particles in complex (shear-dependent) fluids is an important aspect of both natural and industrial flows, for example, pyroclastic gravity currents [1], proppant transport in hydraulic fracturing [2], and fresh cement slurries. Often the suspended phase is (negatively) buoyant and its stability with respect to sedimentation during transport, or after flow cessation [3], is of fundamental interest. Viscoplastic fluids, by virtue of a material yield stress, may support such a coarse particle phase indefinitely. This is governed by a balance between the stress exerted on the fluid by the particle and the fluid yield stress [4], described by the nondimensional yield number $Y = \hat{\tau}_y/(\hat{\rho}_p - \hat{\rho}_f)\hat{\boldsymbol{g}}\hat{l}'$, where $\hat{\boldsymbol{g}}$ is gravitational acceleration, $\hat{\rho}_p$ is the particle density, $\hat{\rho}_f$ the fluid density, $\hat{l}'$ a characteristic length scale, and $\hat{\tau}_y$ the material yield stress. Two aspects of buoyant particle transport in viscoplastic fluids stand out: the conditions for suspension stability, and the sedimentation behavior. Both of these have been well characterized for single particles but not yet for suspensions, particularly under quiescent flow conditions.

With regard to stability, it has been shown that for an isolated particle there exists a critical yield number $Y = Y_0^*$ at which the buoyancy force exerted by the particle is balanced by the fluid yield stress. This has been the subject of many numerical and theoretical works [4–6], and while there is great variability among experimental studies [7,8], the theoretical Y_0^* for a spherical particle has been corroborated by Tabuteau et al. [9]. Given the nonlinear rheology of the suspending fluid a key question is whether Y_0^* is applicable to suspensions. There has been some work, predominantly

*ark44@cam.ac.uk

numerical and experimental, investigating model systems of two or more particles posed in the resistance sense—where flow is driven by a prescribed velocity—rather than the more applicable mobility sense—where flow is driven by applied force—due to the intrinsic numerical and practical difficulties of the latter. It was found that particles near each other, particularly in the inline configuration, experience a decreased drag force, from which it may be inferred that the same configuration would exhibit a higher critical yield number than an isolated particle [10–12]. The theoretical work of Frigaard et al. [13] investigated this critical yield number for suspensions more directly through the out-of-plane flow of uniformly distributed particle suspensions with prescribed uniform suspension velocity. They inferred a volume fraction, ϕ, dependent critical yield number, Y^*_ϕ. However, the resistance formulation has clear drawbacks in that individual particle velocities are prescribed *a priori*. Recently, Chaparian et al. [14] investigated inline particle configurations for up to five particles in the mobility sense, finding not only that their stability criterion is strongly influenced by separation distance but that particle chains are unlikely to be stable sedimentation configurations.

Settling of suspensions in viscoplastic fluids can be categorized as static settling or dynamic settling, depending on the background flow conditions (quiescent in the former). It is well known in the oil industry that background shear enhances settling [15] in shear-thinning fluids. For viscoplastic fluids, Merkak et al. [16] and Ovarlez et al. [17] demonstrated shear-induced settling in fluids regardless of the yield number, showing that particles settle as soon as the fluid yield stress is overcome by macroscopic shear. The latter advocated a suspension settling function, in conjunction with a Newtonian hindering function, incorporating an effective viscosity based on the (applied) macroscopic shear rate. This framework has recently been adopted in a model for solids dispersion in hydraulic fracturing flows [18].

In quiescent background conditions, i.e., in the absence of applied macroscopic shear, a different approach is needed. Single particles settling in viscoplastic fluids under quiescent conditions have been investigated extensively in viscous and inertial regimes, both experimentally and numerically [19–22]. Empirical terminal velocity models have been developed [21,22], and it has been suggested that these may be combined with Newtonian hindering functions in dispersion models such as Kaushal and Tomita [23]. However, studies on suspensions settling in viscoplastic fluids under quiescent conditions are very sparse [24], so whether this is a viable approach is not clear.

In this article we present direct numerical simulations of noncolloidal particle suspensions, in the dilute limit, settling in quiescent viscoplastic fluids. Building on the out-of-plane investigation of Ref. [13], we investigate the stability criterion as a function of solid volume fraction for the in-plane flow and comment on the transition to settling—which, as far as we are aware, has not been investigated previously.

II. MATHEMATICAL FORMULATION AND SOLUTION

In contrast to Newtonian fluids, very little numerical work has been done on suspension sedimentation in viscoplastic fluids. Many successful strategies for large-scale suspension simulation in Newtonian fluids [25] rely on superposition principles to make large-scale computations tractable, which are not applicable to the nonlinear viscoplastic system. Coarse-grain approaches for Newtonian fluids use lubrication force models as subgrid-scale models for the underresolved particle interactions. However, the authors recently found that such lubrication models cannot be straightforwardly applied in cases where particles are strongly confined in their yield envelopes such as may occur in sedimentation without imposed shear [26]. This necessitates direct numerical simulation.

We consider the steady approximation of inertialess, rigid circular particles suspended in incompressible viscoplastic fluid from a mobility perspective. The particles are denoted by P; the particle boundaries by ∂P; and the entire domain (fluid and particle) by Ω; and the far field domain walls by $\partial\Omega$. The fluid has velocity $\hat{\boldsymbol{u}}(\hat{\boldsymbol{x}})$, pressure $\hat{p}(\hat{\boldsymbol{x}})$, plastic viscosity $\hat{\eta}$, and a total stress tensor $\hat{\boldsymbol{\tau}} - \hat{p}\boldsymbol{\delta}$, where variables with a hat are dimensional. In the absence of both fluid and particle inertia, and taking the particle buoyancy, $(\hat{\rho}_p - \hat{\rho}_f)\hat{g}\hat{l}'$, as a characteristic stress scale $\mathcal{T}$—where $\hat{\rho}_p$ and $\hat{\rho}_f$

are the particle and fluid densities, respectively, and $\hat{l}'$ is a characteristic length scale governed by the particle volume to frontal area ratio [10]—we solve the nondimensional steady Stokes equations

$$\nabla \cdot \boldsymbol{\tau} - \nabla p = \frac{\rho_r}{1-\rho_r}\boldsymbol{e}_g, \text{ in } \Omega \setminus P, \quad \nabla \cdot \boldsymbol{u} = 0, \text{ in } \Omega \setminus P, \tag{1}$$

where $\boldsymbol{e}_g$ denotes the unit vector in the direction of gravity, $\rho_r = \hat{\rho}_f/\hat{\rho}_p$ and the particles are negatively buoyant, such that $\rho_r < 1$. We impose no-slip and no-penetration boundary conditions on the domain walls, such that

$$\boldsymbol{u} = 0 \text{ on } \partial\Omega, \tag{2}$$

and the fluid velocity is continuous with that of each particle, such that

$$\boldsymbol{u} \to \boldsymbol{U} + \boldsymbol{\omega} \times (\boldsymbol{x} - \boldsymbol{x}_b) \text{ on } \partial P, \tag{3}$$

where $\boldsymbol{U}$ and $\boldsymbol{\omega}$ are the *a priori* unknown linear and angular particle velocities, $\boldsymbol{x}$ is a point on ∂P, and $\boldsymbol{x}_b$ are the coordinates of the centre of mass of the particle. The particle translational and rotational velocities are determined by satisfying zero force and torque constraints on each particle, $\boldsymbol{F} = 0$, $\boldsymbol{T} = 0$. Here $\boldsymbol{F}$ and $\boldsymbol{T}$ are defined for any given particle by

$$\boldsymbol{F} = \int_{\partial P} (-p\boldsymbol{n} + \boldsymbol{\tau} \cdot \boldsymbol{n})\, ds + \boldsymbol{f}_b, \quad \boldsymbol{T} = \int_{\partial P} (\boldsymbol{x} - \boldsymbol{x}_b) \times (-p\boldsymbol{n} + \boldsymbol{\tau} \cdot \boldsymbol{n})\, ds + \boldsymbol{t}_b, \tag{4}$$

where $\boldsymbol{n}$ is the unit normal vector to the body surface, and $\boldsymbol{f}_b$ and $\boldsymbol{t}_b$ are external body force and torque, respectively.

We close the system using the ideal Bingham constitutive law

$$\begin{aligned} \boldsymbol{\tau} &= \left(1 + \tfrac{Y}{||\dot{\boldsymbol{\gamma}}||}\right)\dot{\boldsymbol{\gamma}} \qquad \text{if } ||\boldsymbol{\tau}|| > Y, \\ \dot{\boldsymbol{\gamma}} &= 0 \qquad\qquad\quad \text{if } ||\boldsymbol{\tau}|| \leqslant Y, \end{aligned} \tag{5}$$

where the rate of strain tensor is defined as $\dot{\boldsymbol{\gamma}} := (\nabla \boldsymbol{u} + \nabla \boldsymbol{u}^{\intercal})$, and $||\cdot||$ is the induced norm of the Frobenius inner product:

$$\boldsymbol{a} : \boldsymbol{b} := \frac{1}{2}\sum_{ij} A_{ij} B_{ij}, \tag{6}$$

such that $||\dot{\boldsymbol{\gamma}}|| = \sqrt{\dot{\boldsymbol{\gamma}} : \dot{\boldsymbol{\gamma}}}$. The force-free and torque-free conditions imply that the particles adjust their velocities and angular velocities instantaneously [27].

Unless otherwise stated, we use $\mathcal{T}/\hat{\eta}\hat{\rho}_f$, $\mathcal{T}\hat{l}'/\hat{\eta}\hat{\rho}_f$, and $\hat{R}$ as characteristic strain $\mathcal{G}$, velocity $\mathcal{V}$, and length $\mathcal{L}$ scales, respectively, where $\hat{R}$ is the particle radius and $\hat{l}' = \pi\hat{R}/2$.

Last, we define the critical yield number at which motion for a suspension of volume fraction ϕ stops as Y^*_ϕ, where for a single particle we find $Y^*_0 = 0.084$, in agreement with the literature [5,14,28] (note that Chaparian et al. [14] use a different length scale in their definition of Y).

We solve (1)–(5) using the widely adopted alternating direction multiplier method—also known as ALG2—developed by Glowinski [29]. It is extensively used in the literature—see Refs. [20,30,31] and references therein—so we do not give details here. We follow the implementation of Refs. [32,33].

Wachs and Frigaard [34] studied the problem numerically for a single sedimenting particle in a Bingham fluid, with a particular focus on the critical yield stress required for cessation of motion. Even with a single particle in two dimensions with a relatively small mesh (61 440 cells), their computations took around 12 h (wall-time). The limiting problem is the high computational expense of the ALG2 algorithm typically used for viscoplastic flow problems; discussion of ALG2 and related algorithms can be found in Refs. [35]. In order to make the larger problem sizes considered in this study tractable we adopt a steady approximation, as in Ref. [14] and employ an overset grid discretization strategy. Briefly, the overset grid method represents a complex domain using

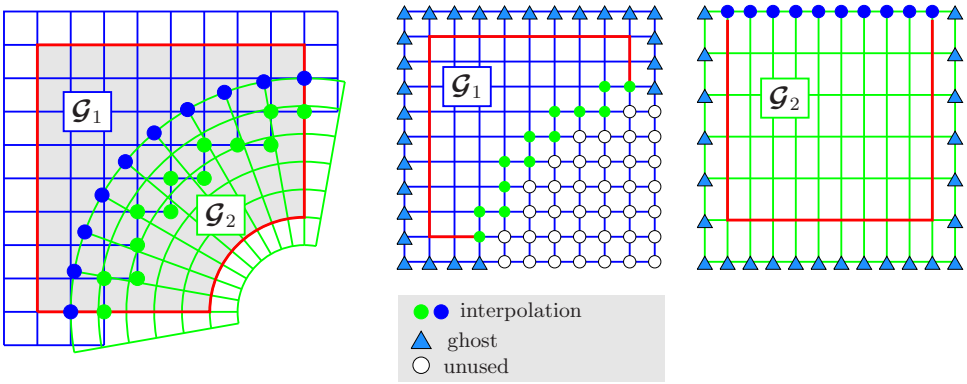

FIG. 1. Left: An overlapping grid consisting of two structured curvilinear component grids, $\boldsymbol{x} = \boldsymbol{\mathcal{G}}_1(\boldsymbol{r})$ and $\boldsymbol{x} = \boldsymbol{\mathcal{G}}_2(\boldsymbol{r})$. Middle and right: Component grids for the square and annular grids in the unit square parameter space $\boldsymbol{r}$. Grid points are classified as discretization points, interpolation points, or unused points. Ghost points are used to apply boundary conditions.

multiple body-fitted curvilinear grids that are allowed to overlap whilst being logically rectangular; see Fig. 1. The overlapping aspect brings flexibility and efficiency to grid generation, which is beneficial for complex domains and moving grid problems. Here, since the cylinders are static, the chief benefit of the overset grid methods is that the grids may be locally refined near the cylinder surfaces while keeping the grids logically rectangular. The grid generation procedure is discussed at length in Refs. [36,37] and has been used for Newtonian and viscoplastic particulate flow problems by the authors in Refs. [26,38]. The resultant linear system is inverted using the MUMPS massively parallel direct linear solver library [39]. Recently some significantly faster algorithms have been developed [40–43], and so we expect a rapid expansion in the near future of the size of problem which can be attempted.

III. RESULTS AND DISCUSSION

We compute the instantaneous velocity field for pseudo-random configurations of infinite circular cylinders, of diameter D, in a confined domain with dimensions $(20\,D, 120\,D)$, for solid volume fractions $\phi = (0.01, 0.05)$ over a yield number range of $Y = (0, 0.173)$. Five pseudo-random configurations are used for each volume fraction.

Figure 2 shows the mean settling velocity of the suspension $\langle \hat{V}_{\phi,Y} \rangle$—normalized by the Stokes velocity of a single particle in a Newtonian fluid $\hat{V}_{0,0}$—averaged over all configurations, for increasing yield number. Here the yield number is normalized using the critical yield number required to hold a single particle at rest, Y_0^*.

All volume fractions show a decrease in settling velocity as the yield number increases. This is expected from Eq. (5) where we can see that for any finite strain rate, a nonzero yield number leads to an increase in the effective viscosity. Looking at the limiting high yield number behavior, we can see that the critical yield number required to hold the suspension at rest, Y_ϕ^* increases with the solid volume fraction, as was found in Frigaard et al. [13] for out-of-plane settling. We find an approximately two-fold increase in the critical yield number for $\phi = 0.05$.

As $Y \to 0$ the medium mirrors a Newtonian fluid with viscosity $\hat{\eta}$, showing hindered settling with increased ϕ [44]. However, for Y sufficiently large, we find higher settling efficiency with increasing solid volume fraction, indicated by the increased mean settling velocity. This is similar to what has been observed in experimental studies of settling suspensions in shear-thinning fluids [45]. There, settling particles shear fluid, causing a local decrease in viscosity and thereby allowing nearby particles to settle more easily.

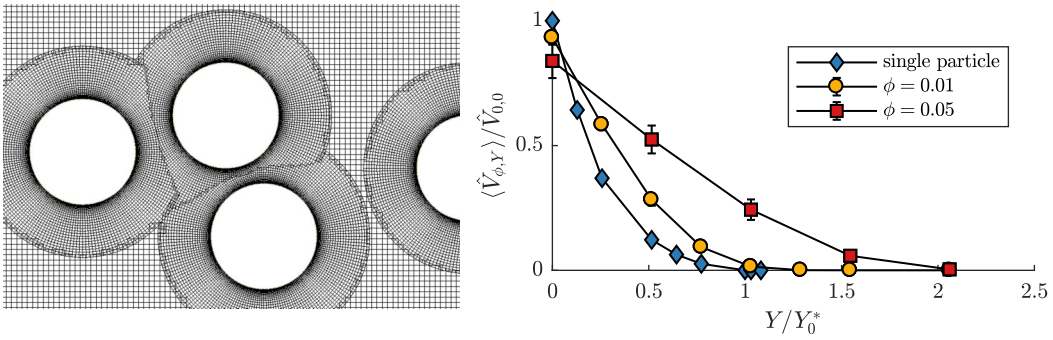

FIG. 2. Left: Close-up view of a representative computational grid used, showing the overlapping particle and background grids and near-surface grid refinement. Right: Mean sedimentation velocity at increasing yield numbers for $\phi = (0, 0.01, 0.05)$, with error bars indicating the standard error of the mean particle sedimentation velocity.

We investigate possible shear thinning by examining the average local viscosity in the vicinity of a particle at a given volume fraction at the same yield number, $Y = 0.043$, where all particles for all volume fractions are mobile. A rectangular grid is placed around each particle in the suspension on which $||\hat{\boldsymbol{\gamma}}||$ is found by means of bilinear interpolation. This is then averaged over all particles in the suspension, and used to find the average local effective viscosity, $\overline{\hat{\eta}}(\langle||\hat{\boldsymbol{\gamma}}||\rangle)$, where $\langle\cdot\rangle$ denotes an average over all particles. This is plotted as color maps in the left panel of Fig. 3. The viscosity field for the single particle is as expected: arbitrarily high viscosity peaks (truncated in the plot) at the unyielded equatorial plugs and the unyielded end caps. As the volume fraction increases the viscosity field becomes more uniform and is found to decrease in magnitude. The viscosity along the two axes of symmetry shown in the $\phi = 0$ plot of Fig. 3 is further examined in the right panel of Fig. 3. The average viscosity decrease with increased solids volume fraction is evident, and the viscosity field is found to be, on average, uniform $\mathcal{L}$ away from the particle surface. Near the surface,

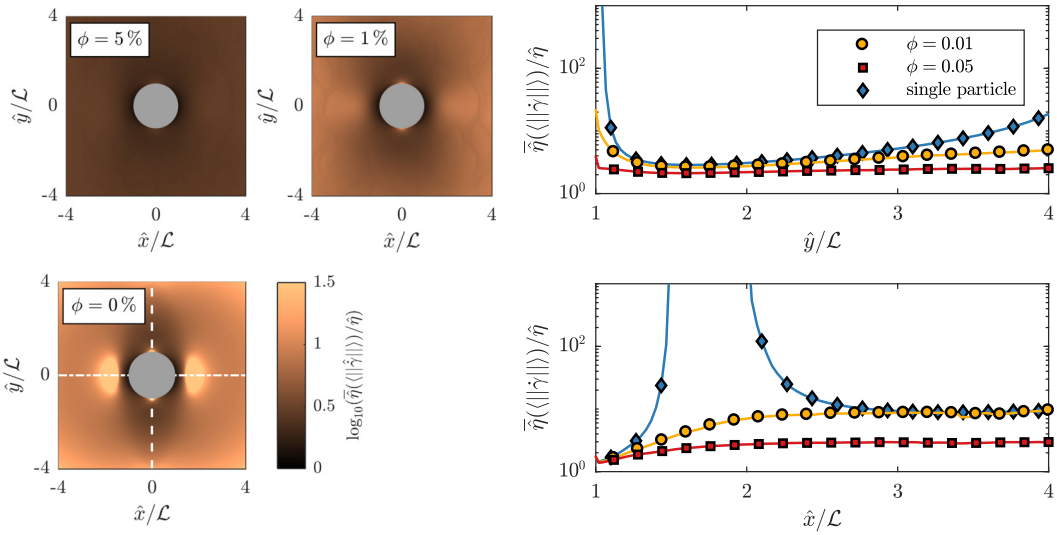

FIG. 3. Left: Average effective viscosity near the particle surface for $Y = 0.043$, with longitudinal (dashed line) and lateral (dash-dot line) axes of symmetries indicated in the $\phi = 0$ panel. Right: Average effective viscosity along the longitudinal (top) and lateral (bottom) axes of symmetry for $Y = 0.043$.

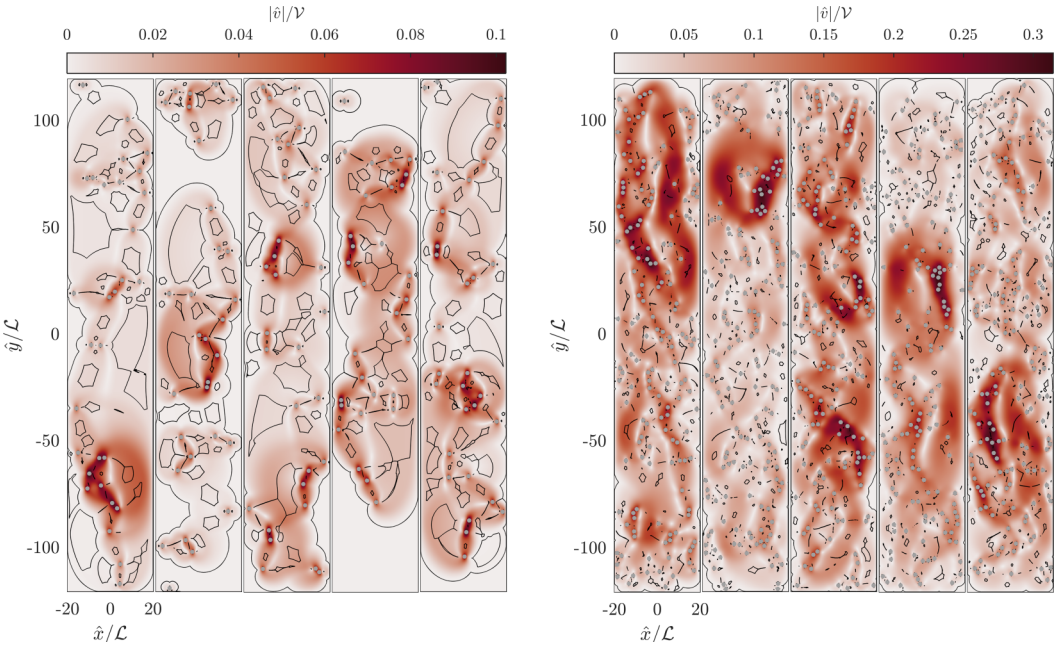

FIG. 4. Color maps of the fluid velocity magnitude with particles overlaid in gray and yield surface indicated by the solid black lines for $Y = 0.087$ with $\phi = 0.01$ (left) and $\phi = 0.05$ (right) for five different configurations.

the viscosity is high in the longitudinal direction due to the attached unyielded end caps; however, in the lateral direction the viscosity is low near the surface due to the viscoplastic boundary layer.

It has been shown experimentally that static suspensions in yield stress fluids will settle when a macroscopic stress, for example by shearing the system, is introduced [16,17]. In the absence of a macroscopic flow, only the buoyancy stress of the individual particles acts on the fluid to drive the flow. Studies of small systems of particles in the resistance formulation demonstrated a drag reduction for inline particle arrangements [10,11,20]. Equivalently, the recent study of Chaparian et al. [14] demonstrated higher velocities for inline configurations in the mobility formulation. The current simulations corroborate this in so far as structures of vertically clustered particles can clearly be visually identified to be settling fastest; for example, see the velocity magnitude color maps in Fig. 4. By examining the velocity field Chaparian et al. [14] demonstrated that nearby particles had little effect on one another beyond a relatively small separation distance $\hat{d}_{\text{sep}}/\mathcal{L} < 20$, suggesting that the stress decay in a viscoplastic fluid is appreciably faster than in a Newtonian fluid where $||\boldsymbol{\tau}|| \sim r^{-1}$ as $r \to \infty$ [46]. As the yield number increases the rapid stress decay becomes more relevant. In the left panel of Fig. 5 the logarithmically scaled color maps of the strain rate magnitude is shown for a configuration of $\phi = 0.01$, with the yield number increasing from left to right. As expected, unyielded material emerges as the yield number increases. For $Y \gtrsim 0.065$ discrete yield envelopes surround particles, coalescing into larger pockets when particles are close together. As the yield number increases further we find clusters of particles inside yield envelopes with comparatively isolated particles held static. For $\phi = 0.05$ we see a similar trend in the $\log_{10}(\dot{\boldsymbol{\gamma}})$ color maps shown in the right panel of Fig. 5. However, there are fewer distinct groups of particles in individual yield envelopes. It is likely that the computational domain is not sufficiently large for a suspension this dense.

We take a closer look at the suspension morphology near Y_0^* in Fig. 4, where color maps of the velocity magnitude with yield surface overlays are shown for all five configurations for $\phi = 0.01$ (left panel) and $\phi = 0.05$ (right panel) at $Y = 0.087$. All configurations for $\phi = 0.01$ show both

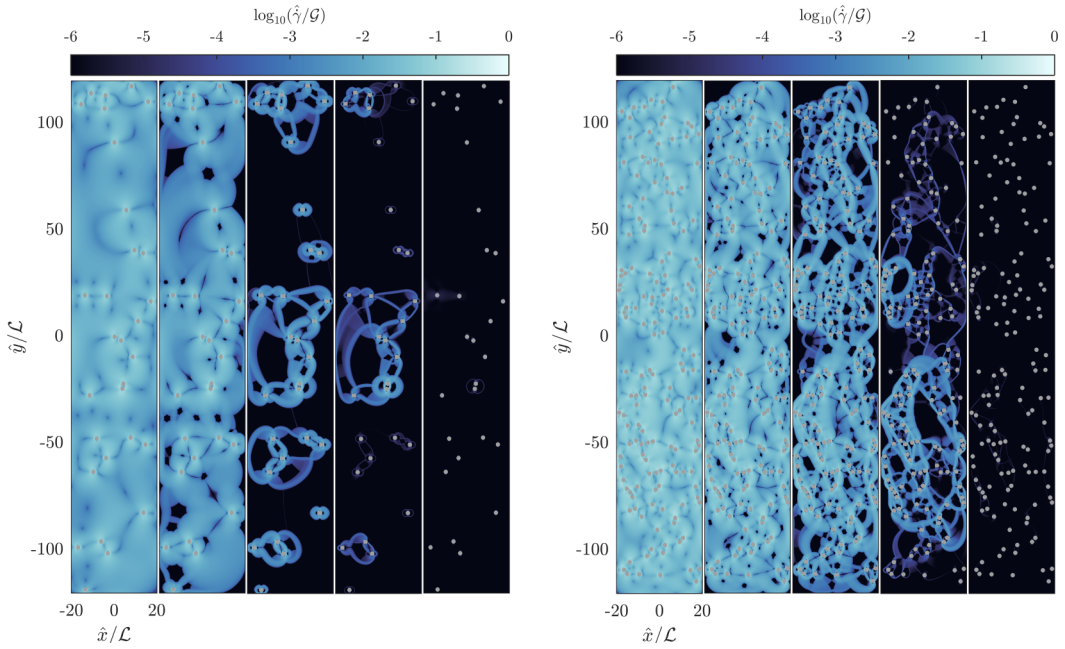

FIG. 5. Color maps of $\log_{10}(\dot{\gamma}/\mathcal{G})$ for $\phi = 0.01$ at $Y = (0, 0.022, 0.065, 0.087, 0.13)$ (left panel) and $\phi = 0.05$ at $Y = (0, 0.043, 0.087, 0.13, 0.17)$ (right panel).

static particles and yield pockets with sedimentation clusters, while for $\phi = 0.05$ no static particles are present in any configuration, and velocity peaks are found near vertically arranged clusters.

This formation of settling pockets of particle-dense regions and isolated static particles is not evident from the mean suspension velocity. In Fig. 6 we show the proportion of settling particles for both volume fractions as the yield number increases, averaged over all configurations. In both cases, for $Y/Y_0^* < 1$ the entire suspension settles as the yield number is below the threshold required to hold even a single particle static. At $Y/Y_0^* \approx 1$ the vast majority of the suspension settles for both cases, with a fraction of static particles evident for $\phi = 0.01$. As the yield number increases beyond $Y/Y_0^* = 1$ more isolated particles are held static, leading to a decrease in the settling fraction for both volume fractions considered. For $\phi = 0.01$ we find that the entire suspension is held static at $Y/Y_0^* \approx 1.5$. The critical yield number required to hold the entire $\phi = 0.05$ suspension static was not reached in this study due to convergence time requirements.

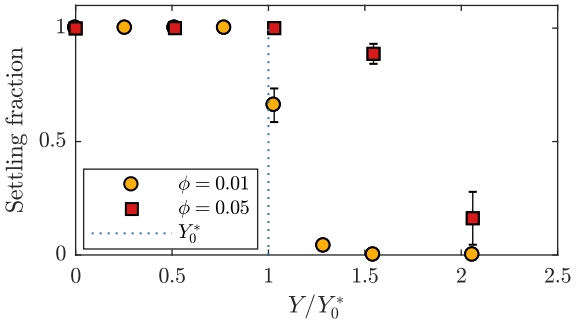

FIG. 6. Proportion of settling particles in the suspension at increasing yield strengths with the critical yield number for a single particle indicated by the dashed line.

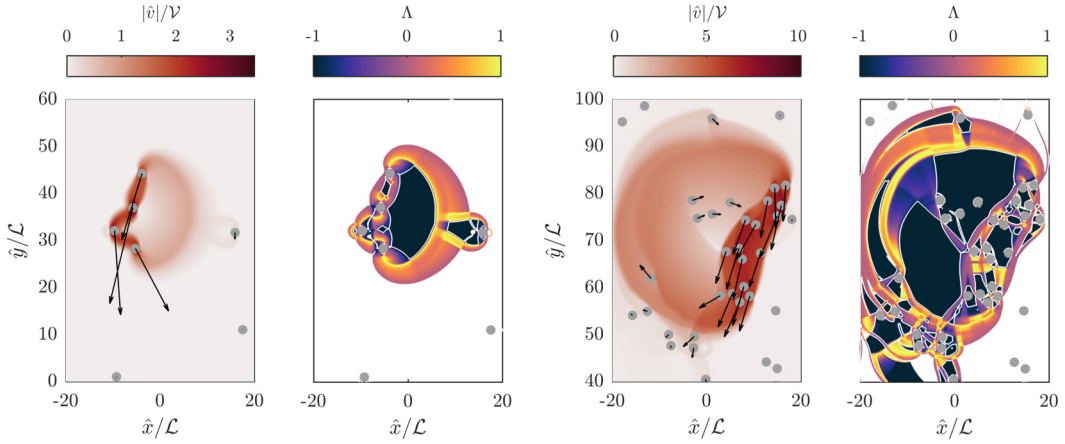

FIG. 7. Examples of the complex flow features found in regime II. Left: Close-up view from a $\phi = 0.01$ suspension with $Y = 0.087$ showing the mobilization of an isolated particle by a passing sedimentation cluster. Right: Close-up view from a $\phi = 0.05$ suspension with $Y = 0.173$ showing lone particles swept up in the strong recirculating flow generated by a sedimentation cluster. A large unyielded region undergoing rigid body motion with embedded particles is visible. For each panel, the left plots show color maps of the fluid velocity magnitude, with particles overlaid in gray and their individual velocity vectors indicated by arrows. The right plots show color maps of the normalized second invariant of the velocity gradient tensor, with static unyielded regions masked off, yield surfaces indicated by the solid white lines, and particles overlaid in gray.

Concentrating on $\phi = 0.01$, for which we have found the critical yield number, we can see three distinct flow regimes: regime I for $0 \leqslant Y < Y_0^*$ where the entire suspension is settling; regime II for $Y_0^* \leqslant Y < Y_\phi^*$ where the proportion of static particles increases as $Y \to Y_\phi^*$; regime III for $Y \geqslant Y_\phi^*$, for which the entire suspension is held stationary. While Y_ϕ^* was not reached for $\phi = 0.05$ in this study we have no reason to believe that the suspension will not be held static with a sufficiently high yield number. Experimental studies have worked with statically held suspensions as dense as $\phi = 0.4$ [17].

In regime I the fluid could be considered as weakly shear-thinning, and regime III is trivial, while in regime II the strong competition between the yield stress and buoyancy of groups of particles leads to complex flow features, which the larger error bars above $Y/Y_0^* > 1$ in Fig. 6 indicate. Two examples of the complex flow features found in this regime are shown in Fig. 7. For each of the two features the left plots show color maps of the fluid velocity magnitude, while the right plots show color maps of the normalized second invariant of the velocity gradient tensor, Λ—a metric used to describe the character of the flow

$$\Lambda = \frac{||\boldsymbol{D}|| - ||\boldsymbol{W}||}{||\boldsymbol{D}|| + ||\boldsymbol{W}||}, \tag{7}$$

where $\boldsymbol{D}$ and $\boldsymbol{W}$ are the symmetric and skew symmetric components of the velocity gradient tensor, $\boldsymbol{D} = 1/2(\nabla \boldsymbol{u} + \nabla \boldsymbol{u}^\intercal)$ and $\boldsymbol{W} = 1/2(\nabla \boldsymbol{u} - \nabla \boldsymbol{u}^\intercal)$, respectively. Negative and positive values of Λ show where flow is dominated by enstrophy and strain, where for $\Lambda = -1$ flow is purely rotational, $\Lambda = 0$ flow undergoes simple shear, and $\Lambda = +1$ flow is purely extensional [47]. The left panel shows a sedimentation cluster in a $\phi = 0.01$ suspension mobilizing a lone particle as it moves past. The right panel is from a $\phi = 0.05$ suspension showing a collection of particles settling together, generating a strong recirculating flow within the yield envelope. Lone particles are swept up by this recirculating flow, and two large unyielded plugs can be seen, one of which has embedded particles that would have otherwise been held static. It is flow features such as these that lead to the larger error bars in Fig. 6 but also complicate the identification of spatial correlation lengths, for example, critical separation distances between particles that encourage settling at yield numbers beyond Y_0^*.

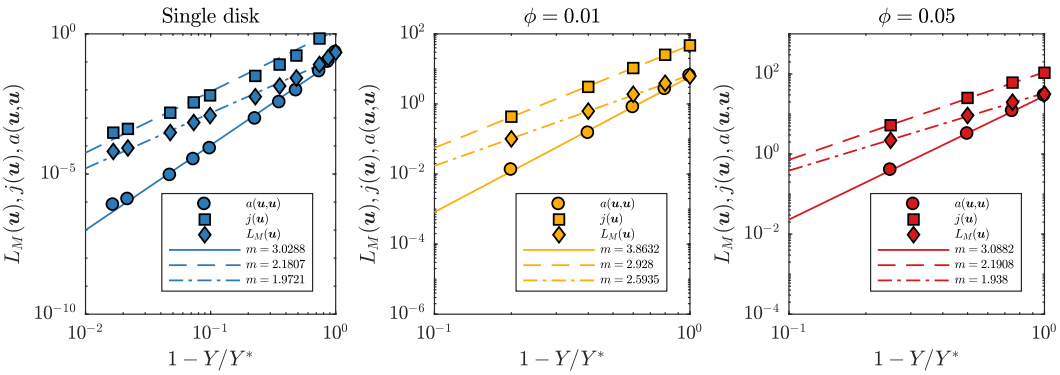

FIG. 8. Convergence behavior of the functionals $a(\boldsymbol{u}, \boldsymbol{u})$ (circles), $j(\boldsymbol{u})$ (squares), and $L(\boldsymbol{u})$ (diamonds), for a single particle (blue), $\phi = 0.01$ (yellow), and $\phi = 0.05$ (red). Symbols are computed, and lines are power-law fits with exponent m.

Following the analysis of Refs. [30,48,49] we examine global flow properties through the viscous dissipation, plastic dissipation and buoyancy work functionals, respectively:

$$a(\boldsymbol{v}, \boldsymbol{w}) = \int_{\Omega \setminus P} \dot{\boldsymbol{\gamma}}(\boldsymbol{v}) : \dot{\boldsymbol{\gamma}}(\boldsymbol{w})\, dA, \quad j(\boldsymbol{v}) = \int_{\Omega \setminus P} ||\dot{\boldsymbol{\gamma}}(\boldsymbol{v})||\, dA, \quad L(\boldsymbol{v}) = \pi \boldsymbol{V} \cdot \boldsymbol{e}_y, \tag{8}$$

where $\boldsymbol{v}$, $\boldsymbol{w}$ are divergence free vector fields satisfying the boundary conditions (2) and (3), and $\boldsymbol{V}$ is a particle velocity vector. Exploring the static stability limit Putz and Frigaard [48] observed that as $Y \to Y^{*-}$:

$$a(\boldsymbol{u}, \boldsymbol{u}) \sim O([Y^* - Y]^2), \tag{9}$$

$$Yj(\boldsymbol{u}) \sim L(\boldsymbol{u}) \sim O(Y^* - Y), \tag{10}$$

where $O([Y^* - Y]^2)$ is a lower bound on the decay rate of the viscous dissipation [49], but it always decays faster than the plastic dissipation [48]. In the following analysis, we approximate the critical yield numbers for the suspensions as $Y^*_{0.01} \approx 1.5Y^*_0$ and $Y^*_{0.05} \approx 2Y^*_0$, respectively.

The panels of Fig. 8 show the convergence of the functionals for $\phi \in \{0, 0.01, 0.05\}$. For all volume fractions explored here, the viscous dissipation decays faster than $O([Y^* - Y]^2)$, the plastic dissipation approximately one order of magnitude slower and at a similar rate to the buoyancy work functional.

Defining the particle Bingham number as $B = \hat{\tau}_y \hat{L}/\hat{\mu}\hat{U}_p$, where $\hat{U}_p$ is a particle settling velocity, Chaparian and Frigaard [30] linked the mobility and resistance formulation by rescaling variables by Y/B, showing that $Y \to Y^{*-}$ and $B \to \infty$ are the same limit and are coupled by

$$B \sim (1 - Y/Y^*)^{-\nu}, \tag{11}$$

where ν is some positive exponent.

Using the mean suspension velocity (at a given volume fraction) to compute a $B(\phi)$ we show the convergence at large B in Fig. 9, along with a power-law fit to the single disk data. For the single disk, fitting the power law to the markers for $1 - Y/Y^* < 0.5$ to limit ourselves to the behavior near the yield limit [48], we recover $\nu \approx 2$, in line with previous results of Tokpavi et al. [5] and Chaparian and Frigaard [30]. For the suspensions it is evident that we lack data sufficiently close to Y^*_ϕ to explore the behavior near the yield limit. More computations near the yield limit are required for the suspensions. However, this is a far more computational demanding task than for single disks, as for single disks the resistance problem—which is significantly cheaper—may be evaluated at arbitrary velocities (see Chaparian and Frigaard [30]) while for the suspensions we must evaluate

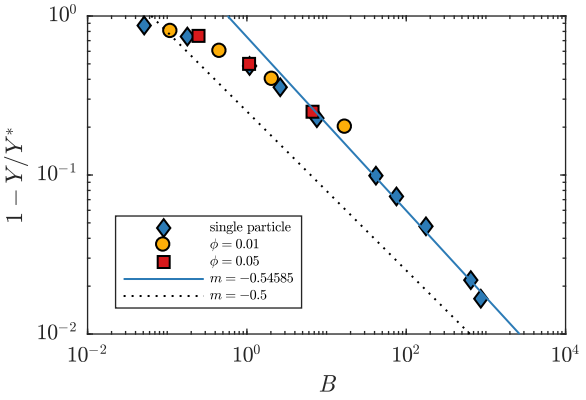

FIG. 9. Convergence at large B for three volume fractions. Symbols are computed, and lines are power-law fits with exponent m.

the mobility problem. This, coupled with the necessarily increased problem size for the suspensions, makes further exploration of the near yield limit behavior a computationally arduous task.

We can take a closer look at the energy dissipation in our system by examining the local viscous dissipation, $\Phi = \boldsymbol{\tau} : \boldsymbol{D}$, in various flow structures by utilizing the normalized second invariant of the velocity gradient tensor, Λ, discussed previously. In Fig. 10 we show the viscous dissipation per unit volume as a function of the flow parameter Λ for a single disk and the suspensions. Defining a shear flow as $-1/3 \leqslant \Lambda \leqslant 1/3$ [50], we can see that for a single disk most viscous dissipation is confined to shear layers, at all Y. For a single disk at low Y there is some contribution from extensional flow regions. However, as Y increases, the viscous dissipation becomes confined to shear layers, as is evidenced by the steepening in the left-hand side of the Φ peak near $\Lambda = 0$. For the two suspensions the viscous dissipation peaks in the shear layers, and the Φ peak steepens up as Y increases. However, unlike for the single disk, contributions to the viscous dissipation from extensional flow regions remain significant, particularly for $\phi = 0.05$.

In Fig. 11 we plot probability density functions of Λ. For the single disk, the flow is initially dominated by extensional flow. As Y increases, the particle becomes enclosed by a yield envelope, with shear layers developing on the envelope interface. This is reflected as a decrease in the extensional component, and the development of a peak near $\Lambda = 0$. Increasing the yield number further results in the growth of unyielded plugs on either side of the particle, with additional shear layers between the particle and plug, and plug and yield envelope wall, leading to a rapid decrease

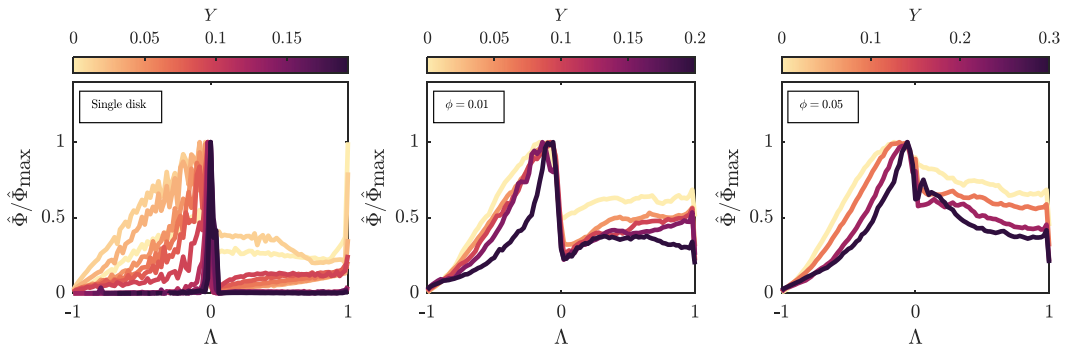

FIG. 10. Normalized energy density per unit volume per unit Λ for a single disk (left), $\phi = 0.01$ (middle), and $\phi = 0.05$ (right).

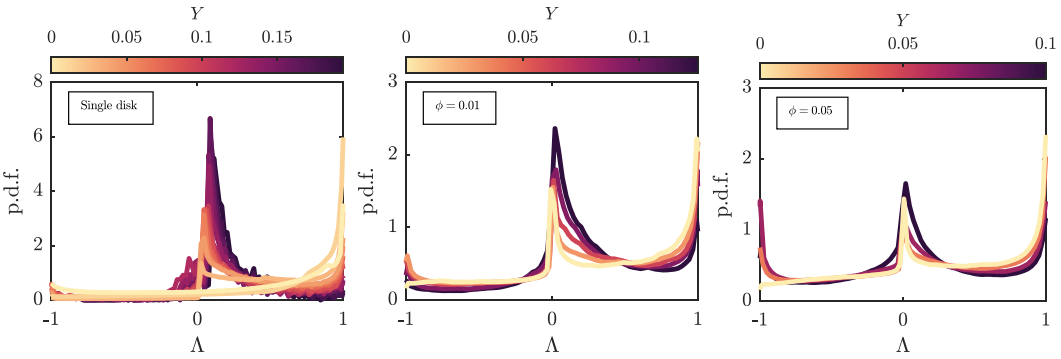

FIG. 11. Probability density functions of Λ with increasing Y for a single disk (left), $\phi = 0.01$ (middle), and $\phi = 0.05$ (right).

in extensional flow and a large peak near $\Lambda = 0$. We can see that for a single particle, the limiting flow, as $Y \to Y^{*-}$, is dominated by shear layers.

For the suspensions the trend is similar, with shear layers increasing while extensional flow decreases as Y increases. While we do not have enough data close enough to Y^*_ϕ to determine the limiting flow characteristics, the trend is certainly indicative of a shear-dominated flow near Y^*_ϕ. In light of this, it is possible that with more data near Y^*_ϕ, the power-law behavior in Fig. 9 should approach that of the single disk, i.e., $\nu \approx 2$, in line with other flows dominated by simple shear [30,49,51].

IV. CONCLUSIONS

In this article we investigated settling of two-dimensional noncolloidal particles in viscoplastic fluids under quiescent conditions by means of direct numerical simulation. Three flow regimes were identified, where (I) the entire suspension settles, (II) there exist both static and settling particles in the same suspension, and (III) the entire suspension is arrested.

In regime I for sufficiently high yield numbers we observe enhanced settling with increased volume fraction, opposite to a Newtonian fluid, which we attribute to shear-thinning. Regime II displays complex flow features such as sedimenting clusters, mobilization of lone particles, and rigid recirculating zones. For suspension volume fractions greater than zero the transition to regime III is delayed, requiring a higher yield number to hold the suspension static than is required to hold a single particle static. This corroborates the theoretical work of Frigaard et al. [13] and the inferences drawn from studies of small-scale model systems [10,14].

Further research is required to explore the dynamics of the settling phases in regimes I and II. Regime II is of particular interest since it may lead to heterogeneities in the suspension. Understanding this regime and the transition to regime III may play a role in explaining observations in many industrial and natural problems involving the sedimentation of viscoplastic suspensions under quiescent flow conditions. We anticipate that new solution methods [40–43] will soon enable much larger simulations of such systems, including the ability to investigate time evolution and inertia, which were neglected in this study. Finally, we encourage researchers to investigate this problem experimentally.

ACKNOWLEDGMENTS

The authors are grateful to the referees for their invaluable comments and suggestions, which helped to improve the paper's quality greatly. A.R.K. acknowledges financial support from the Engineering and Physical Sciences Research Council (EPSRC) Centre for Doctoral Training in Computational Methods for Materials Science under Grant No. EPSRC EP/L015552/1. This work was supported by Schlumberger Cambridge Research Limited.

[1] J. Dufek, The fluid mechanics of pyroclastic density currents, Annu. Rev. Fluid Mech. **48**, 459 (2016).
[2] A. A. Osiptsov, Fluid mechanics of hydraulic fracturing: A review, J. Petrol. Sci. Eng. **156**, 513 (2017).
[3] N. B. C. Santos, F. M. Fagundes, F. de Oliveira Arouca, and J. J. R. Damasceno, Sedimentation of solids in drilling fluids used in oil well drilling operations, J. Petrol. Sci. Eng. **162**, 137 (2018).
[4] A. N. Beris, J. H. Tsamopoulos, R. C. Armstrong, and R. A. Brown, Creeping motion of a sphere through a Bingham plastic, J. Fluid Mech. **158**, 219 (1985).
[5] D. L. Tokpavi, A. Magnin, and P. Jay, Very slow flow of Bingham viscoplastic fluid around a circular cylinder, J. Non-Newtonian Fluid Mech. **154**, 65 (2008).
[6] L. Jossic and A. Magnin, Drag and stability of objects in a yield stress fluid, AIChE **47**, 2666 (2001).
[7] H. Emady, M. Caggioni, and P. Spicer, Colloidal microstructure effects on particle sedimentation in yield stress fluids, J. Rheol. **57**, 1761 (2013).
[8] R. P. Chhabra, *Bubbles, Drops, and Particles in Non-Newtonian Fluids*, 2nd ed. (Taylor & Francis, Boca Raton, Florida, 2007).
[9] H. Tabuteau, F. K. Oppong, J. R. de Bruyn, and P. Coussot, Drag on a sphere moving through an aging system, Europhys. Lett. **78**, 68007 (2007).
[10] D. L. Tokpavi, P. Jay, and A. Magnin, Interaction between two circular cylinders in slow flow of Bingham viscoplastic fluid, J. Non-Newtonian Fluid Mech. **157**, 175 (2009).
[11] B. T. Liu, S. J. Muller, and M. M. Denn, Interactions of two rigid spheres translating collinearly in creeping flow in a Bingham material, J. Non-Newtonian Fluid Mech. **113**, 49 (2003).
[12] P. Jie and Z. Ke-Qin, Drag force of interacting coaxial spheres in viscoplastic fluids, J. Non-Newtonian Fluid Mech. **135**, 83 (2006).
[13] I. A. Frigaard, J. A. Iglesias, G. Mercier, C. Pöschl, and O. Scherzer, Critical yield numbers of rigid particles settling in Bingham fluids and Cheeger sets, SIAM J. Appl. Math. **77**, 638 (2017).
[14] E. Chaparian, A. Wachs, and I. A. Frigaard, Inline motion and hydrodynamic interaction of 2D particles in a viscoplastic fluid, Phys. Fluids **30**, 033101 (2018).
[15] L. H. Childs, A. J. Hogg, and D. Pritchard, Dynamic settling of particles in shear flows of shear-thinning fluids, J. Non-Newtonian Fluid Mech. **238**, 158 (2016).
[16] O. Merkak, L. Jossic, and A. Magnin, Migration and sedimentation of spherical particles in a yield stress fluid flowing in a horizontal cylindrical pipe, AIChE **55**, 2515 (2009).
[17] G. Ovarlez, F. Bertrand, P. Coussot, and X. Chateau, Shear-induced sedimentation in yield stress fluids, J. Non-Newtonian Fluid Mech. **177–178**, 19 (2012).
[18] S. Hormozi and I. A. Frigaard, Dispersion of solids in fracturing flows of yield stress fluids, J. Fluid Mech. **830**, 93 (2017).
[19] D. D. Atapattu, R. P. Chhabra, and P. H. T. Uhlherr, Wall effects for spheres falling at small Reynolds number in a viscoplastic medium, J. Non-Newtonian Fluid Mech. **38**, 31 (1990).
[20] Z. Yu and A. Wachs, A fictitious domain method for dynamic simulation of particle sedimentation in Bingham fluids, J. Non-Newtonian Fluid Mech. **145**, 78 (2007).
[21] K. C. Wilson, R. R. Horsley, T. Kealy, J. A. Reizes, and M. Horsley, Direct prediction of fall velocities in non-Newtonian materials, Int. J. Miner. Process. **71**, 17 (2003).
[22] A. S. Arabi and R. S. Sanders, Particle terminal settling velocities in non-Newtonian viscoplastic fluids, Can. J. Chem. Eng. **94**, 1092 (2016).
[23] D. R. Kaushal and Y. Tomita, Prediction of concentration distribution in pipeline flow of highly concentrated slurry, Part. Sci. Tech. **31**, 28 (2013).
[24] N. P. Khabazi, K. Sadeghy, and S. M. Taghavi, Simulating particle sedimentation in yield stress fluids, in *24th International Congress of Theoretical and Applied Mechanics (ICTAM), Montreal, Canada* (2016).
[25] J. F. Brady, Stokesian dynamics, Annu. Rev. Fluid Mech. **20**, 111 (1988).
[26] A. R. Koblitz, S. Lovett, and N. Nikiforakis, Viscoplastic squeeze flow between two identical infinite circular cylinders, Phys. Rev. Fluids **3**, 023301 (2018).
[27] J. Feng and D. D. Joseph, The unsteady motion of solid bodies in creeping flows, J. Fluid Mech. **303**, 83 (1995).
[28] M. F. Randolph and G. T. Houlsby, The limiting pressure on a circular pile loaded laterally in cohesive soil, Geotechnique **34**, 613 (1984).

[29] R. Glowinski, *Numerical Methods for Non-linear Variational Problems* (Springer Verlag, Berlin, Heidelberg, New York, Tokyo, 1984).
[30] E. Chaparian and I. A. Frigaard, Yield limit analysis of particles motion in a yield-stress fluid, J. Fluid Mech. **819**, 311 (2017).
[31] L. Muravleva, Squeeze plane flow of viscoplastic Bingham material, J. Non-Newtonian Fluid Mech. **220**, 148 (2015).
[32] M. A. Olshanskii, Analysis of semi-staggered finite-difference method with application to Bingham flows, Comput. Methods Appl. Mech. Eng. **198**, 975 (2009).
[33] E. A. Muravleva and M. A. Olshanskii, Two finite-difference schemes for calculation of Bingham fluid flows in a cavity, Russ. J. Numer. Anal. Math. Model. **23**, 615 (2008).
[34] A. Wachs and I. A. Frigaard, Particle settling in yield stress fluids: Limiting time, distance and applications, J. Non-Newtonian Fluid Mech. **238**, 189 (2016).
[35] R. Glowinski, On alternating direction methods of multipliers: A historical perspective, CMAS **34**, 59 (2014).
[36] G. S. Chesshire and W. D. Henshaw, Composite overlapping meshes for the solution of partial differential equations, J. Comput. Phys. **90**, 1 (1990).
[37] W. D. Henshaw, Ogen: an overlapping grid generator for Overture, Research Report UCRL-MA-132237, Lawrence Livermore National Laboratory (1998).
[38] A. R. Koblitz, S. Lovett, N. Nikiforakis, and W. D. Henshaw, Direct numerical simulation of particulate flows with an overset grid method, J. Comput. Phys. **343**, 414 (2017).
[39] P. R. Amestoy, I. S. Duff, J. L'Excellent, and J. Koster, A fully asynchronous multifrontal solver using distributed dynamic scheduling, SIAM J. Matrix Anal. Appl. **32**, 15 (2001).
[40] P. Saramito, A damped Newton algorithm for computing viscoplastic fluid flows, J. Non-Newtonian Fluid Mech. **238**, 6 (2016).
[41] T. Treskatis, M. Moyers-González, and C. J. Price, An accelerated dual proximal gradient method for applications in viscoplasticity, J. Non-Newtonian Fluid Mech. **238**, 115 (2016).
[42] J. Bleyer, Advances in the simulation of viscoplastic fluid flows using interior-point methods, Comput. Methods Appl. Mech. Eng. **330**, 368 (2018).
[43] Y. Dimakopolous, G. Makrigiorgos, G. C. Georgiou, and J. Tsamopoulos, The PAL (Penalized Augmented Lagrangian) method for computing viscoplastic flows: A new fast converging scheme, J. Non-Newtonian Fluid Mech. **256**, 23 (2018).
[44] J. F. Richardson and W. N. Zaki, Sedimentation and fluidisation. Part 1. Trans. Inst. Chem. Eng. **32**, 35 (1954).
[45] B. A. Moreira, F. de Oliveira Arouca, and J. J. R. Damasceno, Analysis of suspension sedimentation in fluids with rehological shear-thinning properties and thixotropic effects, Powder Tech. **308**, 290 (2017).
[46] R. I. Tanner, Stokes paradox for power-law flow around a cylinder, J. Non-Newtonian Fluid Mech. **50**, 217 (1993).
[47] E. J. Hemingway, A. Clarke, J. R. A. Pearson, and S. M. Fielding, Thickening of viscoelastic flow in a model porous medium, J. Non-Newtonian Fluid Mech. **251**, 56 (2018).
[48] A. Putz and I. A. Frigaard, Creeping flow around particles in a Bingham fluid, J. Non-Newtonian Fluid Mech. **165**, 263 (2010).
[49] A. Roustaei, T. Chevalier, L. Talon, and I. A. Frigaard, Non-Darcy effects in fracture flows of a yield stress fluid, J. Fluid Mech. **805**, 222 (2016).
[50] S. De, J. A. M. Kuipers, E. A. J. F. Peters, and J. T. Padding, Viscoelastic flow simulations in model porous media, Phys. Rev. Fluids **2**, 053303 (2017).
[51] I. A. Frigaard and O. Scherzer, The effects of yield stress variation on uniaxial exchange flows of two Bingham fluids in a pipe, SIAM J. Appl. Math. **60**, 1950 (2000).